An unprecedented 3D Eu(III)-organic framework built of imidazole carboxylate by *in situ* reaction

In recent decades, metal-organic frameworks (MOFs) have appealed to researchers in the fields of gas adsorption[1], catalysis[2], luminescence[3], magnetism[4], porosity[5], proton conductivity[6,7], degradation of nerve agents to fuel cells[8], and so on. Nevertheless, synthesizing MOFs with expectant structures and desired properties is still a difficult task for researchers. From a large number of previous reports, people found that, to design and prepare the multifunctional organic ligands is a useful way to obtain the desired MOFs. 1*H*-imidazol-4,5-dicarboxylate (H_3IDC)[6] indicates strong coordination ability in the preparations of porous and helical MOFs. Some complexes with H_3IDC have been reported[9–11]. However, the MOFs built by the organic ligand 1*H*-imidazole-4-carboxylic acid (H_2IMC) produced from the *in situ* decarboxylation of H_3IDC was seldom investigated[12], especially, the rare-earth metal complexes based on H_2IMC. Indeed, only several complexes, $[Cu^{II}(phen)(HIMC)(H_2O)]·[Cu^{II}(phen)-(HIMC)(NO_3)]·NO_3·H_2O$ (phen = 1,10-phenanthroline monohydrate) and $[Cu^{II}(2,2'-bipy)-(HIMC)]·NO_3·xH_2O$ (2,2'-bipy = 2,2'-dipyridyl)[13], $[Cd(HIMC)_2(H_2O)]_n$, $[Cd(HIMC)_2]_n$ (ref. 14), and $[Gd(HIMC)(SO_4)(H_2O)]$ (refs 15–18) have been found in the literature.

Promoted by the above considerations, we hope to prepare more related lanthanide-based MOFs from H_2IMC by *in situ* decarboxylation of H_3IDC. Fortunately, we get one novel 3D Eu-MOF, $[Eu_5(IMC)_4(C_2O_4)_{3.5}]_n$ (**1**) by solvothermal reaction of H_3IDC and $(NH_4)_2C_2O_4$ with Eu^{3+} salt. It is to be pointed out that we have attempted to use H_2IMC directly to react with Eu(III) ion and wanted to obtain (**1**), but were unsuccessful. That is to say, *in situ* reaction is essential in the synthesis of (**1**).

Here we report the synthesis (note 1) and crystal architecture of (**1**). (**1**) is a 3D porosity (note 2) and crystallizes in the *I*-4 space group. The symmetric unit of compound (**1**) is composed of four IMC^{2-} ligands, and three and a half chelating $C_2O_4^{2-}$ ligands, and five Eu(III) ions (Figure 1). The central Eu1(III) atom is 9-coordinated by O1, O2, O3, O4, O5A, O6A and O6B atoms from two $C_2O_4^{2-}$

and three IMC^{2-} anions, while two N atoms are derived from two diverse IMC^{2-} ligands. Coordination environment of Eu2(III) ion is different from that of Eu1(III) ion, which is twelve-coordinated by four oxygen and eight nitrogen atoms, and all atoms are from the organic ligands (Figure 1). Bond angles surrounding the Eu(III) are in the range of 17.2(3)–156.2(3)°. The Eu-O distances range from 2.331(12) to 2.445(10) Å, while the Eu-N distances vary from 2.413(7) to 2.471(17) Å (Supplementary Table 1), being consistent with the values of typical ranges reported for the other Eu(III) complexes[19,20]. In the 3D structure of 1 each organic ligand adopts a μ_3-kO : kO' : kN mode to connect Eu(III) ions (Supplementary Figure 1). Additionally, three neighbouring Eu(III) atoms are connected by organic ligands forming a 1D gyro chain which are bridged by μ_2-$C_2O_4^{2-}$ auxiliary li-

gands producing a layer with quadrilateral elements (Supplementary Figure 2). Furthermore, oxalate ligands connect the layers to a rare kranze anatomy 3D structure. The complex with inner diameter of 1.056 nm was measured by diamond 3.1. As seen, the topology of (**1**) was obtained by the program TOPOS on the basis of experimental CIF file (Figure 2).

As discussed earlier, Sun *et al.*[12] suggested that under hydrothermal conditions the Cu(II) performs a catalytic function in the decarboxylation process for H_3IDC. We think that under solvothermal conditions here, the europium(III) also displays a catalytic function.

We could not obtain crystalline (**1**), when the preparation reaction was performed without ammonium oxalate, suggesting that $C_2O_4^{2-}$ is significant in the formation of (**1**). If $Eu(NO_3)_3$ is changed to $Eu_2(C_2O_4)_3$, the crystalline solids of (**1**) could also be produced.
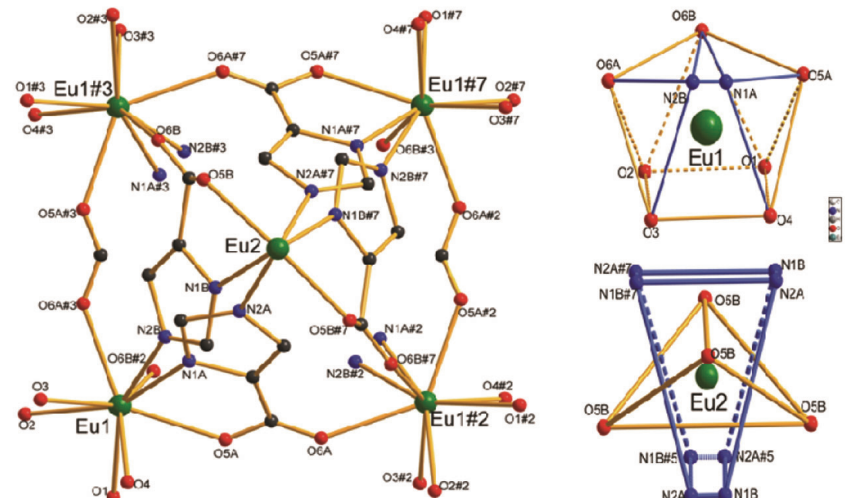

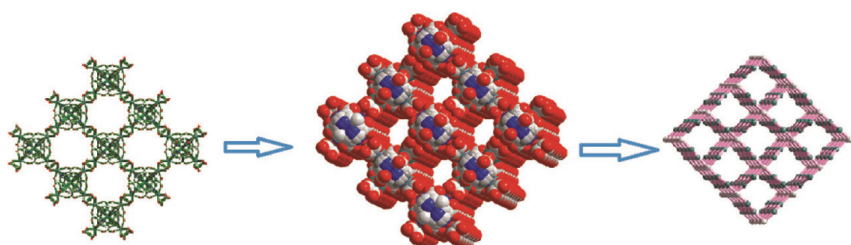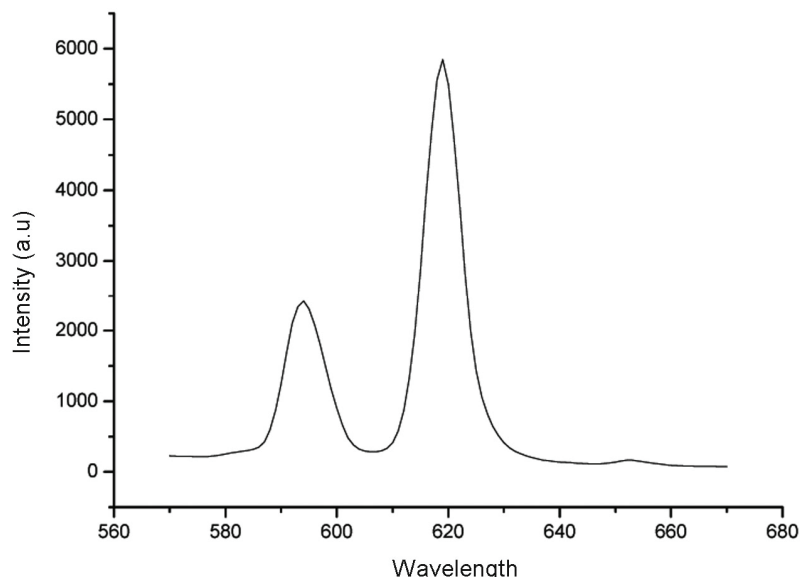**Figure 1.** Coordination environments of Eu^{3+} atoms in (**1**) (H atoms omitted for clarity).

Figure 2. Crystal structure and topology analysis of (**1**).

Figure 3. The fluorescence spectrum of compound (**1**).

Characteristic absorption bands of COO^-, N–H bond and water molecules can be discovered in infrared spectrum of (**1**) (Supplementary Figure 2). The strong and broad absorption bands ranging from 3000 to 3450 cm^{-1} show ν_{O-H} and ν_{N-H}, the stretching frequencies. The strong absorption bands from 1400 to 1800 cm^{-1} are assigned to ν_{COO^-} vibrations for the carboxyl groups.

To characterize the MOF thoroughly for thermal stability, thermogravimetric (TG) analysis was studied in air (Supplementary Figure 4). The TG curve indicates two steps of weight loss. From 74.7°C to 301.1°C, the loss of two oxalate ions of 11.90% can be observed (calcd. 11.34%). Then pyrolysis of IMC^{2-} ligands and remaining oxalate ions from 301.1°C to 835°C occurred. The final residue is 2.5 Eu_2O_3 (obs. 58.78%; calcd. 56.68%).

The X-ray powder diffraction (PXRD) pattern of 1 is consistent with the simulated one from crystal data (Supplementary Figure 5) suggesting its high phase purity.

Eu-based MOFs usually indicate outstanding luminescent properties[21,22]. Solid-state luminescent properties of (**1**) were explored at 25°C. As shown in Figure 3, (**1**) indicates characteristic Eu(III) emission. The strong emission peaks at 595 and 617 nm under excitation at 340 nm can be ascribed to $^5D_0 \rightarrow {}^7F_1$ and $^5D_0 \rightarrow {}^7F_2$ transitions respectively[23,24].

The former corresponds to a magnetic dipole transition. The latter is a hypersensitive transition[25]. Obviously, the population of the excited states of Eu(III) atom can be increased by coordination to IMC^{2-} ligands, which act as sensitizers like 'antenna effect'.

In summary, we get a novel kranze anatomy Eu-MOF through the H_3IDC ligand and rare-earth ion by *in situ* reaction. Compound (**1**) was characterized by single crystal X-ray diffraction, elemental analysis and infrared spectroscopy. The results demonstrate that the simple flexible organic ligand can fine-tune its configuration to satisfy the geometric requirement of the metal atoms, and has the potential function for synthesizing more new MOFs. The complex (**1**) exhibits excellent fluorescence property suggesting potential applications in luminescent materials.

Appendix A. Supplementary data: CCDC 1542590 contains the supplementary crystallographic data for this paper. The data can be obtained free of charge from The Cambridge Crystallographic Data Centre via www.ccdc.cam.ac.uk/data_request/cif.

Notes

1. Nitrate Europium (0.1 mmol), NaOH (0.1 mmol), ammonium oxalate (0.1 mmol), and H_3IDC (0.1 mmol) was firstly dissolved in a mixed solution of ethanol and water (1 : 6; 7.0 ml); trimethylamine (about 0.6 mmol) was then added to adjust pH between 9 and 10 with vigorous stirring to achieve sufficient dissolution. The resulting mixed solution was were sealed in a 25 ml Teflon jar bomb and heated at 180°C for 72 h. The reaction mixture was then allowed to cool to 25°C. Colourless cube-shaped crystals were appeared. Washed with water and dried in air (43% yield based on Eu). Calcd for $C_{24}H_8N_8O_{24}Eu_5$: C, 18.51; H, 0.52; N, 7.17%. Found: C, 18.65; H, 0.58; N, 7.46%. IR (cm^{-1}, KBr): 3445 (m), 1621 (s), 1567 (m), 1464 (s), 1389 (s), 1315 (s), 1243 (w), 1104 (m), 861 (s), 828(w), 800 (m), 670 (s), 534 (w).

2. Crystal data for **1**: $a = 18.4611$ (3) Å, $b = 184611(3)$ Å, $c = 10.0713$ (3) Å, $\alpha = 90.00°$, $\beta = 91.055$ (2)°, $\gamma = 90.00°$, V = 3432.42 (13) $Å^3$, $Z = 4$, $fw = 1552.18$, GOF = 1.092, $R_1 = 0.0448$, $wR_2 = 0.1235$, crystal size $= 0.32 \times 0.26 \times 0.23$ mm, Dc = 1.502 $Mg\ m^{-3}$ $\mu = 4.558\ mm^{-1}$, reflns collected/unique = 11146/3026, $R(int) = 0.0598$.

1. Su, X., Bromberg, L., Martis, V., Simeon, F., Huq, A. and Hatton, T. A., *ACS Appl. Mater. Interf.*, 2017, **12**, 11299–11306.
2. Shen, K., Chen, X. D., Chen, J. Y. and Li, Y. W., *ACS Catal.*, 2016, **6**, 5887–5903.
3. Zhang, J., Zhao, L. L., Liu, Y. X., Li, M. Y., Li, G. and Meng, X. R., *New J. Chem.*, 2018, **42**, 6839–6847.
4. Jia, H. L., Li, Z. F., Chen, Q. and Li, G., *Supramole. Chem.*, 2015, **27**, 613–619.
5. Zhang, Y. Y., Shen, X. Y., Weng, L. H. and Jin, G. X., *J. Am. Chem. Soc.*, 2014, **136**, 15521–15524.
6. Liu, R. L., Zhao, L. L., Dai, W., Yang, C. L., Liang, X. and Li, G., *Inorg. Chem.*, 2018, **57**, 1474–1482.
7. Liang, X., Li, B., Wang, M. H., Wang, J., Liu, R. L. and Li, G., *ACS Appl. Mater. Interf.*, 2017, **9**, 25082–25086.
8. Khan, I. A., Qian, Y. H., Badshah, A., Nadeem, M. A. and Zhao, D., *ACS Appl. Mater. Interf.*, 2016, **27**, 17268–17275.
9. Lu, W. G., Zhong, D. C., Jiang, L. and Lu, T. B., *Cryst. Growth Des.*, 2012, **12**, 3675–3683.
10. Zhou, W. Y., Zhao, L. J., An, Z. L. and Li, G., *Polyhedron*, 2016, **117**, 202–208.
11. Chen, W. Y., Wang, J., Zhao, L. L., Dai, W., Li, Z. F. and Li, G., *J. Alloy. Compd.*, 2018, **750**, 895–901.
12. Sun, Y. Q., Zhang, J. and Yang, G. Y., *Chem. Commun.*, 2006, **18**, 1947–1949.
13. Cheng, Y. F., Lu, X. M. and Wang, G., *Dalton Trans.*, 2014, **43**, 5357–5363.
14. Cai, S. L., Pan, M., Zheng, S. R., Tan, J. B., Fan, J. and Zhang, W. G., *Cryst. Eng. Comm.*, 2012, **14**, 2308–2315.

15. Sun, Y. Q., Zhang, J. and Yang, G. Y., *Chem. Commun.*, 2010, **46**, 1947–1949.
16. Sun, Y. G. *et al.*, *J. Coord. Chem.*, 2010, **63**, 4188–4200.
17. Sun, Y. Q. and Yang, G. Y., *Dalton Trans.*, 2007, **34**, 3771–3781.
18. Gryz, M. Starosta, W. and Leciejewicz, J., *J. Coord. Chem.*, 2007, **60**, 539–546.
19. Gao, R. M., Wang, F., Zhong, Y. H. and Li, G., *Supramole. Chem.*, 2016, **28**, 204–211.
20. Shi, B. B., Zhong, Y. H., Guo, L. L. and Li, G., *Dalton Trans.*, 2015, **44**, 4362–4369.
21. Bünzli, J. C. G. and Piguet, C., *Chem. Rev.*, 2002, **15**, 1897–1928.
22. Bünzli, J. C. G., *Chem. Rev.*, 2010, **12**, 2729–2755.
23. Binnemans, K., *Chem. Rev.*, 2009, **109**, 4283–4374.
24. Escribano, P., López, B. J., Aragó, J. P., Cordoncillo, E., Viana, B. and Sanchez, C., *J. Mater. Chem.*, 2008, **18**, 23–40.
25. Guo, M.-W., Chen, N., Gao, Y.-C., Lu, H.-J. and Li, G., *J. Coord. Chem.*, 2012, **65**, 1724–1739.

QIUYING HUANG[1]
LILI ZHAO[2]
ZIFENG LI[2]
GANG LI[2,*]

[1]Department of Chemical Engineering,
Henan Polytechnic Institute,
Nanyang 473000, P. R. China
[2]College of Chemistry and Molecular
  Engineering,
Zhengzhou University,
Zhengzhou 450001, Henan, P. R. China
*For correspondence.
e-mail: gangli@zzu.edu.cn

Comparison of stress azimuth data derived by geogenic electromagnetic radiation technique and from the analysis of exhumation joints

During the last decade, considerable progress has been made to understand the cause and nature of electromagnetic emission anomalies that precede major earthquakes[1,2]. Based on field measurements using a portable instrument, the preferred orientations of geogenic electromagnetic radiation (EMR), especially the principal directions of radiation have been proved to be reproducible and are related to the stress field of the lithosphere[3–6]. Thus, the geogenic electromagnetic emission could be an important precursor of active deformation of the earth's crust[7,8]. Although it is a fairly new technique in the geoscience arena, there are some examples where EMR was used to decipher crustal stress orientations. Using this technique, maximum principal horizontal stress azimuth of N103°E was measured in the Upper Rhine Graben near the Odenwald mountains in Germany[5]. In the Kachchh region of western India, EMR yielded a mean SH_{max} (maximum horizontal stress) azimuth of N60°E (ref. 6). This technique is also used for quantitative measurement of stresses inside a tunnel. The azimuth for the major principal horizontal stress was calculated to be N143°E around the Feuerberg tunnel in Germany[3]. The technique was also used to decipher the horizontal stress azimuth in the Lower Muschelkalk region of Northern Baden-Württemberg, Germany[4]. The mean SH_{max} azimuth was calculated to be N137°E, which tallies with the *in situ* stress measurements calculated using other techniques.

Exhumation joints have been classically used by geologists to decipher the direction of recent stresses and those during uplift[9]. Conjugate exhumation joints develop due to shear failure of a rock when it relaxes during its uplift or later in response to the recent stresses. Acute bisector of a conjugate joint set can indicate the direction of maximum stress. If the joints are observed on a horizontal bedding plane and the joint faces are vertical, the derived stress azimuth can indicate the direction of maximum horizontal stress (SH_{max}) or the direction of maximum compression.

In this study, we have derived SH_{max} azimuth in a geological site near Bhopal, India using both methods mentioned above, and compared the corresponding results. The similarities observed in the results corroborate for the accuracy of the EMR technique in such applications. As location-specific stress data are relatively scarce, the results should encourage scientists to adopt the EMR technique for recent surface stress estimation. The site was chosen because Bhopal is situated in the heart of stable continental Indian peninsula and away from any known active fault; hence the derived stress orientation should represent that of the regional stress and possibly have not been modified by pre-existing discontinuities. The exposed rocks around Bhopal are either Deccan basalt or sandstone equivalent to Rewa or Bhander group from the Vindhyan super group. The rocks are exposed as inliers and are geomorphically distributed in small hills in and around the city of Bhopal.

The emission of low-frequency electromagnetic signals associated with rock fracturing has been essentially attributed to the concept of the earth's crust acting as charging electric battery under increasing strain, analogous to the concept of piezoelectricity. The electric charges are released by activation of dormant charge carriers in the oxygen anion sublattice (peroxy bonds or positive hole pairs). The intermittent and erratic occurrences of EM signals are the results of increasing build-up of the charges in the earth's crust. They get released when crack networks percolate through the stressed rock volumes as a result of onset of nucleation[8]. The damage zone at the tip of an existing fracture consists of multiple microcracks with high stress concentrations oriented with respect to the fracture zone. Since nanocracks and microcracks are the sources of geogenic EMR emission, it is possible to determine the high stress regions or zones by measuring EMR being emitted much before any macroscopic failure[10]. EMR associated with microcracks was observed in all kinds of rocks as well as in glass, ceramics, metals and ice[11–14]. Since fracture propagation is always accompanied by microcrack formation, initiation of an active movement along a